Topological Crystalline Insulator Candidate ErAsS with Hourglass Fermion and Magnetic-Tuned Topological Phase Transition

Hongxiang Chen, Jiacheng Gao, Long Chen, Gang Wang,* Hang Li, Yulong Wang, Juanjuan Liu, Jinchen Wang, Daiyu Geng, Qinghua Zhang, Jieming Sheng, Feng Ye, Tian Qian, Lan Chen, Hongming Weng,* Jie Ma,* and Xiaolong Chen*

Topological crystalline insulators (TCIs) with hourglass fermion surface state have attracted a lot of attention and are further enriched by crystalline symmetries and magnetic order. Here, the emergence of hourglass fermion surface state and exotic phases in the newly discovered, air-stable ErAsS single crystals are shown. In the paramagnetic phase, ErAsS is expected to be a TCI with hourglass fermion surface state protected by the nonsymmorphic symmetry. Dirac-cone-like bands and nearly linear dispersions in large energy range are experimentally observed, consistent well with theoretical calculations. Below $T_N \approx 3.27$ K, ErAsS enters a collinear antiferromagnetic state, which is a trivial insulator breaking the time-reversal symmetry. An intermediate incommensurate magnetic state appears in a narrow temperature range (3.27–3.65 K), exhibiting an abrupt change in magnetic coupling. The results reveal that ErAsS is an experimentally available TCI candidate and provide a unique platform to understand the formation of hourglass fermion surface state and explore magnetic-tuned topological phase transitions.

1. Introduction

Exploring novel topological materials and related phase transitions has been a central research theme in condensed matter physics and material science[1–3] stimulated by the potential application of dissipationless, gapless edge states and the significance of finding exotic quantum phases or quasiparticles. Among them, topological materials with nontrivial anti-band crossings have attracted much attention. For example, the relativistic Weyl or Dirac fermions are found to exist around the twofold- or fourfold-degenerated anti-band crossings near the Fermi level (E_F),[4–7] resulting in exotic surface states and novel quantum responses including 3D Hall effect,[8] chiral anomaly magnetoresistance,[9] and large second

H. Chen, J. Gao, L. Chen, G. Wang, Y. Wang, D. Geng, Q. Zhang, T. Qian, L. Chen, H. Weng, X. Chen
Beijing National Laboratory for Condensed Matter Physics
Institute of Physics
Chinese Academy of Sciences
Beijing 100190, China
E-mail: gangwang@iphy.ac.cn; hmweng@iphy.ac.cn; xlchen@iphy.ac.cn
H. Chen
School of Materials Science and Engineering
Fujian University of Technology
Fuzhou 350118, China
J. Gao, L. Chen, G. Wang, Y. Wang, D. Geng, T. Qian, L. Chen, H. Weng, X. Chen
University of Chinese Academy of Sciences
Beijing 100049, China
G. Wang, T. Qian, L. Chen, H. Weng, X. Chen
Songshan Lake Materials Laboratory
Dongguan, Guangdong 523808, China
H. Li
Photon Science Division
Paul Scherrer Institute
Forschungsstrasse 111, Villigen-PSI 5232, Switzerland

J. Liu, J. Wang
Department of Physics and Beijing Key Laboratory of Opto-electronic Functional Materials & Micro-Nano Devices
Renmin University of China
Beijing 100872, China
J. Sheng
Academy for Advanced Interdisciplinary Studies
Southern University of Science and Technology
Shenzhen 518055, China
J. Sheng
Department of Physics
Southern University of Science and Technology
Shenzhen 518055, China
F. Ye
Neutron Scattering Division
Oak Ridge National Laboratory
Oak Ridge, TN 37831, USA
J. Ma
Key Laboratory of Artificial Structures and Quantum Control
Shenyang National Laboratory for Materials Science
School of Physics and Astronomy
Shanghai Jiao Tong University
Shanghai 200240, China
E-mail: jma3@sjtu.edu.cn

ADVANCED
SCIENCE NEWS
www.advancedsciencenews.com

ADVANCED
MATERIALS
www.advmat.de

harmonic generation effect.[10,11] Hourglass fermion surface state locating at the vertex in the neck of an hourglass-like dispersion, enables exploration of remarkable topological phases, such as the hourglass Weyl point,[12] movement along high symmetry lines,[13] and hourglass nodal chains[14] or net.[15] By introducing nonsymmorphic symmetry-preserved inter-layer couplings, hourglass fermion surface state in topological crystalline insulators (TCIs) can be obtained.[16–19] For example, hourglass-like dispersion was predicted to exist in nonsymmorphic TCIs KHgX (X = As, Sb, and Bi),[20] and some experimental evidence of hourglass fermion surface state has been observed in KHgSb.[21] Layered compounds M_3SiTe_6 (M = Nb, Ta) were predicted to have a fourfold-degenerated hourglass Dirac loop formed by a collection of hourglass band-crossing points that are protected by inter-layer nonsymmorphic symmetry.[22,23] Besides, 3D bulk systems like perovskite iridates[24] and some oxides[12,14,15] with nonsymmorphic symmetry were also discussed to have possible hourglass dispersion. However, hourglass fermion surface states are rarely verified for the drawbacks including air-sensitivity, miscellaneous band dispersions cross E_F, and challenging of cleavage in the candidates mentioned above. Thus, it is highly desired to discover suitable candidate materials with hourglass fermion surface states to explore their intriguing properties and new topological phases.

In the view of layer construction (LC)[18,19] scheme, the 3D bulk systems with hourglass fermion surface state can be constituted by the glide symmetry related 2D topological insulators (TI). In realistic materials, some special atomic planes would have nontrivial band inversion, which can be looked as the effective 2D TI planes. In contrast to the accidental band inversion in Dirac semimetals including Cd_3As_2 and Na_3Bi caused by low-lying 6s (or 5s) atomic orbitals,[6,7] the delocalized π bonds originated from the p orbitals in the square net are responsible for the large band inversion energy, and in turn cause the essential band inversion and clean Fermi surface with a large linear energy range near E_F.[25,26] Because of the essential band inversion and large linear band dispersion, square-net sublattice formed by single element could be suitable to construct candidate materials having hourglass fermion surface states, which both guarantee the existence of 2D TI and convenience for experimental observation.[25,26] Not only exotic properties like 2D spin–orbital Dirac points,[27,28] extremely large magnetoresistance,[29] and electron–hole tunneling[30] are predicted and observed in square-net-contained materials,[31] but also hourglass fermion surface state can be realized by stacking these 2D TIs with nonsymmorphic symmetry.[16] With proper in-plane lattice distortion, the hourglass fermion surface state has been theoretically demonstrated to exist in orthorhombic LaSbTe with zig-zag Sb-atom layers stacking along the a axis with nonsymmorphic symmetry.[32] However, orthorhombic LaSbTe has not become experimentally available so far, rather tetragonal LaSbTe and La-substituted RESbTe (RE = rare earth) have been reported in literatures.[33–38]

Here, we report the discovery of air-stable orthorhombic ErAsS, aiming at investigating the possible hourglass fermion surface state and the interplay between magnetism and topology.[39–44] The prepared ErAsS crystallizes in a space group $Pnma$ (No. 62), exhibiting in-plane distorted zig-zag-arranged As-atom layers. Neighboring zig-zag-arranged

As-atom layers stagger along the a axis with nonsymmorphic symmetry, and Er atoms form a 3D spin-frustrated system due to the distortion. A collinear antiferromagnetic (AFM) state was detected below Néel temperature ($T_N \approx 3.27$ K) by the single-crystal neutron diffraction, accompanied with an intermediate incommensurate magnetic state with $T_{ICM} \approx 3.65$ K. The electronic structure for paramagnetic (PM) ErAsS shows a clean Fermi surface and a wide energy range linear bands with Dirac-like anti-band crossings near E_F determined by angle-resolved photoemission spectroscopy (ARPES) and scanning tunneling microscopy/spectroscopy (STM/STS). An hourglass fermion surface state and 1D hinge states are predicted to exist in PM ErAsS, protected by the nonsymmorphic symmetry connecting two As-atom layers, whereas the collinear AFM state having four As-atom layers is a trivial insulator for breaking both nonsymmorphic symmetry and time-reversal symmetry (TRS). These results show a new and experimentally available TCI candidate with hourglass fermion surface state and exotic phases, tuned by magnetic structure from the PM state to the AFM ground state through an intermediate incommensurate magnetic state, demonstrating the potential of deeply investigating the hourglass fermion surface state and the interplay between magnetism and topology in ErAsS.

2. Results and Discussion

2.1. Crystal Structure

ErAsS crystallizes in an orthorhombic space group $Pnma$ (No. 62) with $a = 16.7493(12)$ Å, $b = 3.7782$ (2) Å, $c = 3.8087(2)$ Å (Table S1, Supporting Information). As shown in **Figure 1**a, the crystal structure is composed of the alternating stacking of ErS bilayer and As-atom single layer along the a axis. Different from the perfect square-net Si plane in ZrSiS,[26] the As atoms are zig-zag arranged in the As-atom plane of ErAsS, between which the nearest-neighbor distance $l_1 = 2.529(3)$ Å and the next-nearest-neighbor distance $l_2 = 2.842(3)$ Å. The distortion in As-atom plane can be evaluated by $\delta_{As} = 2(l_1 - l_2)/(l_1 + l_2) = 11.66\%$, larger than that in Sb-atom plane (9.71%) of supposed orthorhombic LaSbTe.[32] Two neighboring zig-zag-arranged As-atom layers stagger along the a axis by orientating 180° each other with nonsymmorphic symmetry, including the a-glide mirror plane perpendicular to the c axis and the twofold screw axis along the a axis and sliding $a/2$ (Figure 1a).

Due to the distortion, Er atoms form a rectangular-net plane with the nearest distance ($d_1 = 3.7798(4)$ Å) and the next-nearest distance ($d_2 = 3.8027(4)$ Å) between intra-layer Er atoms, in which the distortion can be evaluated by $\delta_{Er} = 2(d_1 - d_2)/(d_1 + d_2) = 0.60\%$, close to the distortion ($\delta_{La} = 0.57\%$) of La-atom plane in supposed orthorhombic LaSbTe.[32] Considering the intrinsic moment of Er and the third-nearest distance ($d_3 = 4.4058(14)$ Å) between Er atoms (the nearest distance between inter-layer Er atoms) (Figure 1c), Er atoms form a 3D spin-frustrated system due to the distortion, which would host various magnetic states in contrast to supposed orthorhombic LaSbTe.[32]

Consequently, both Er and As atoms are not located at the high-symmetry positions, causing the space group to transform
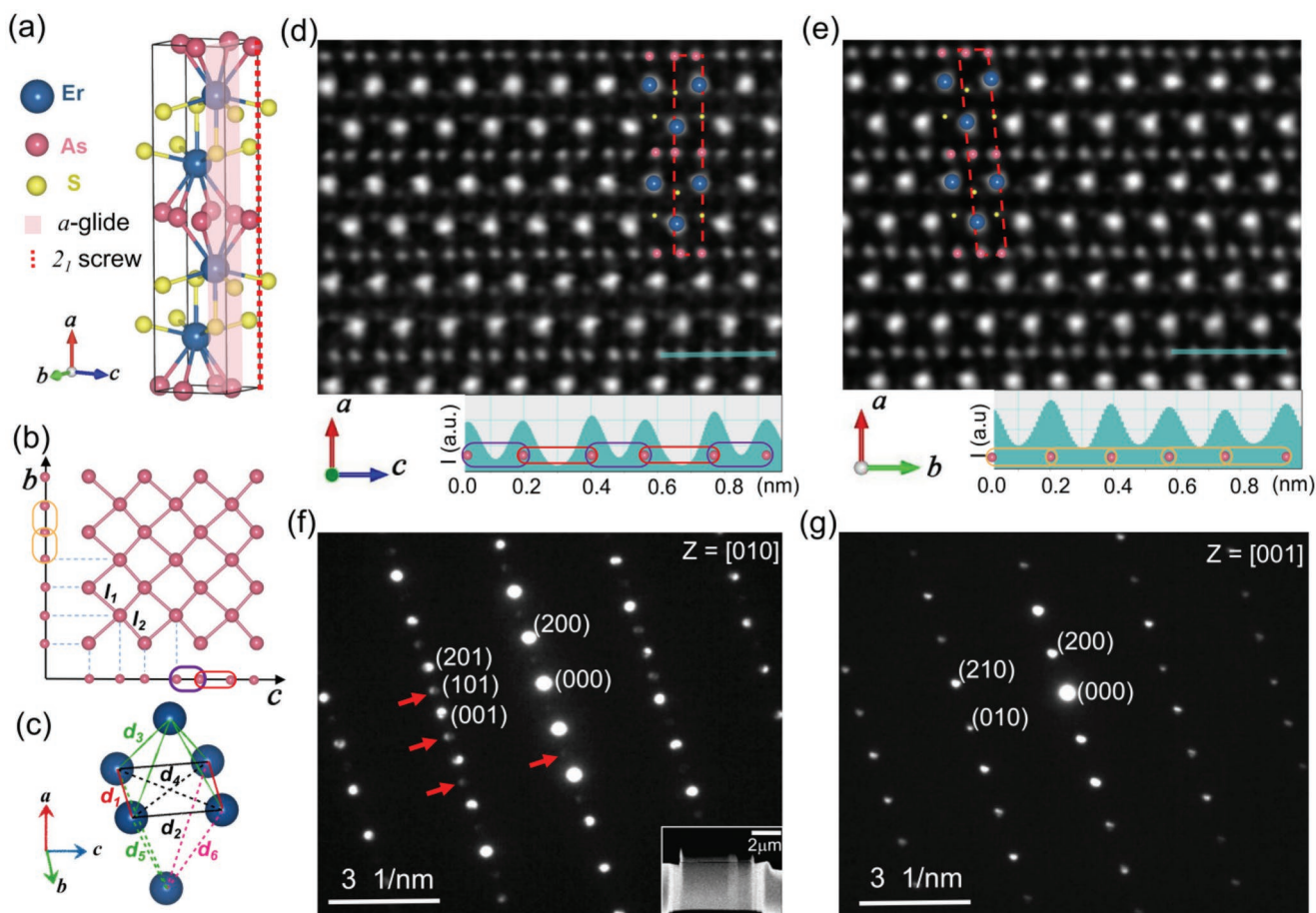
**ADVANCED
SCIENCE NEWS**

www.advancedsciencenews.com

**ADVANCED
MATERIALS**

www.advmat.de

Figure 1. Crystal structure of ErAsS. a) Schematic crystal structure of ErAsS at room temperature and inter-layer nonsymmorphic symmetry. b) Atomic arrangement of single As-atom layer viewed along the *a* axis and the corresponding atomic arrangement of As atoms on the *b* and *c* axes. c) Arrangement and distance of neighboring Er atoms. The HAADF images collected along the d) *b* and e) *c* axes, where the blue, red, and yellow balls represent Er, As, and S atoms, respectively. The lower insets are the corresponding intensity and position of As atoms along the green lines. The FFT SEAD patterns of ErAsS along the f) [010] and g) [001] axes. The red arrows indicate the (*h0l*) (*h* = odd integer) peaks and the inset shows the thin lamella of ErAsS.

from tetragonal *P4/nmm* (No. 129) with C_4 in-plane symmetry into orthorhombic *Pnma* (No. 62) with C_2 in-plane symmetry. Thus, orthorhombic ErAsS owns three screw axes, two glide planes perpendicular to the *a* and *c* axes, and one mirror plane perpendicular to the *b* axis.

The crystal structure is further confirmed by the high-angle annular-dark-field (HAADF) (Figure 1d,e) using scanning transmission electron microscopy (STEM). Note that As atoms have equal spacing along the *b* axis but different spacing along the *c* axis, consistent with the zig-zag-arranged As-atom layer (Figure 1b), therefore excluding the possibility of the previously reported monoclinic ErAsS where As atoms would show different spacing along both the *b* and *c* axes.[45] The inequality of As atom arrangement between the *b* and *c* axes shows a C_2 in-plane symmetry. Meanwhile, the existence of (*h0l*) (*h* = odd integer) peaks in the fast Fourier transform (FFT) selected area electron diffraction (SEAD) pattern along the *b* axis (Figure 1f), also confirms the orthorhombic crystal structure (see Figure S1 and Tables S1 and S2, Supporting Information, for more details of crystal structure determination).

2.2. Magnetic Structures

Figure 2 shows the temperature-dependent magnetic states of ErAsS determined by the single-crystal neutron diffraction in the (H0L) scattering plane. As shown in Figure 2a, a series of magnetic reflections at (H+1/2, 0, L+1/2) with wavevector $\mathbf{q} = 1/2(a^* + c^*)$ (a^* and c^* are the reciprocal lattice vectors) can be clearly observed at 2.22 K compared with the PM phase (Figure 2c). Through the symmetry analysis according to the magnetic wavevector and space group *Pnma*, ErAsS forms a collinear AFM state with an ordering moment of 8.8 μ_B/Er parallel to the *b* axis (See Figure S2, Supporting Information, for refinement details). The magnetic unit cell is doubled along both the *a* and *c* axes (Figure 2d), which can be attributed to the distortion-induced magnetocrystalline anisotropy energy.[46] Consequently, only the mirror plane perpendicular to the *b* axis and the screw axis along the *b* axis remains in collinear AFM ErAsS. The TRS $\mathcal{T}$ followed by a translation along the *c* axis forms a new anti-unitary symmetry operation $\mathcal{S} = \mathcal{T}\left\{00\frac{1}{2}\right\}$; thus the magnetic space group is P_a2_1/m.
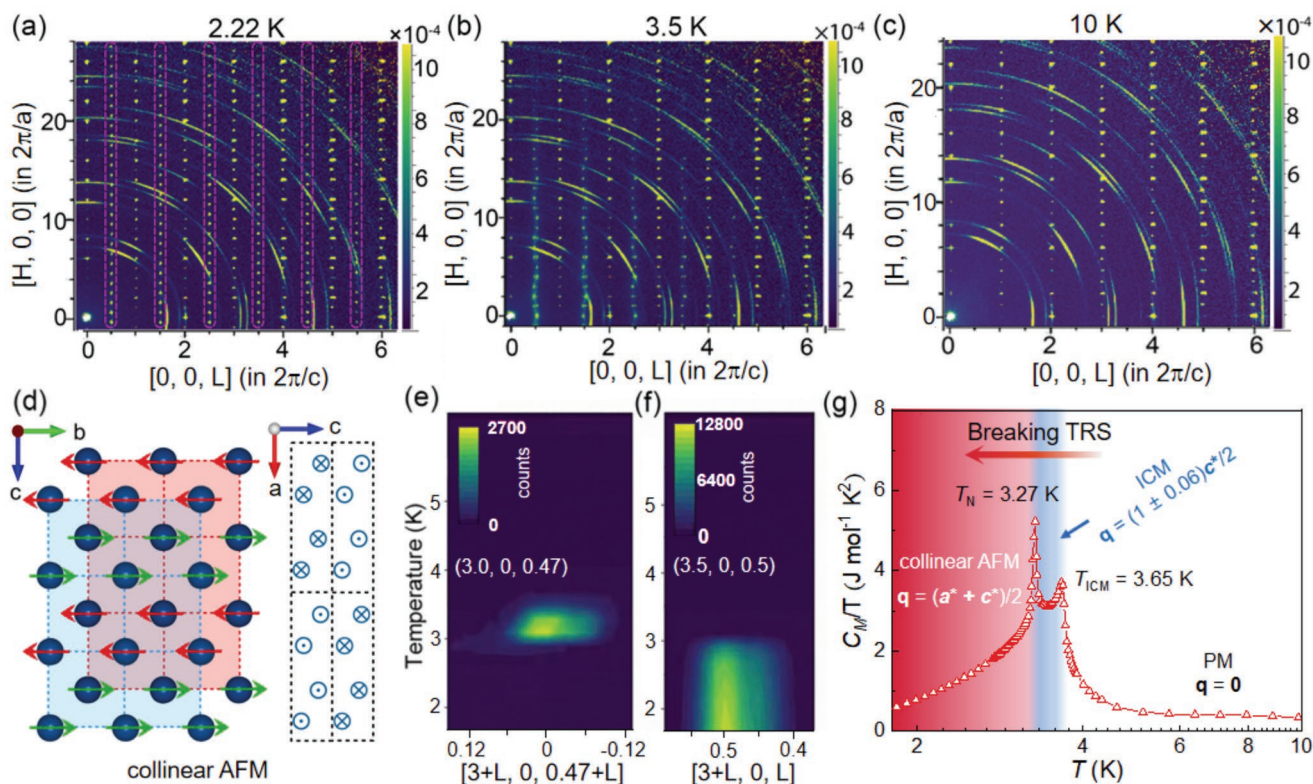
Figure 2. Magnetic structures determined from neutron diffraction. The contour plots of diffraction patterns in the (H0L) reciprocal plane at a) 2.22 K, b) 3.5 K, and c) 10 K. d) The collinear AFM ordering in a ErS bilayer viewed along the a axis and in a magnetic unit cell along the b axis. The blue and red rectangular nets indicate the upper and lower layer of Er atoms in a ErS bilayer, respectively. The black dotted rectangular denotes the unit cell of PM ErAsS. The temperature-dependent intensity of magnetic peaks at e) (3.0, 0, 0.47) and f) (3.5, 0, 0.5). g) The magnetic phase diagram. The red triangular represents the temperature-dependent C_M/T, where C_M is the specific heat contribution of magnetism by subtracting the contribution of crystal lattice.

At 3.5 K, new series of magnetic peaks around (H, 0, L+1/2) are presented in the contour plots of diffraction pattern in the (H0L) reciprocal plane as shown in Figure 2b. The positions and intensities of these magnetic peaks seem to be modulated differently along different directions. Along (00L), the split peaks at (H, 0, L+1/2(1 ± δ)) are evident by subtracting the background of 10 K (Figure S3, Supporting Information), indicating an incommensurate magnetic state with modulation wavevectors $q = 1/2(1 ± \delta)c^*$, where $\delta = 0.06$ represents a small deviation from the integer ratio. This results in a characteristic incommensurate magnetic wavevector $q = (0, 0, 0.47)$. Along (H00), there exists a wavelike modulation in the incommensurate magnetic peak intensity with additional diffuse scattering. A similar feature has been observed in RE_2BaNiO_5 (RE = Er and Tm),[47] and is interpreted as sinusoidal structures with amplitude-modulated moments.[48] The positions of diffuse scattering can be fitted with a sine/cosine function and possibly give a wavelike modulated magnetic moment $M\cos(2\pi Kr)$ along the a axis, where K is the propagation vector[49] but cannot be easily determined in this case.

Figure 2e,f shows the temperature-dependent intensity of corresponding magnetic peaks. The intensity of the incommensurate magnetic peak at (3.0, 0, 0.47) sharply increases around 3.6 K and then decreases at 3.0 K, whereas the collinear AFM magnetic peak at (3.5, 0, 0.5) emerges below 3.0 K with five times larger saturated intensity. Such difference of intensity

can be understood within the average effect on the moment amplitude of Er by the wavelike modulation. These two magnetic phases were also identified from the magnetic susceptibility and specific heat capacity measurements (Figure S4, Supporting Information). Therefore, an evolution from the high-temperature PM phase to the collinear AFM state with $q = 1/2(a^* + c^*)$ through an intermediate wavelike modulated incommensurate magnetic state with $q = 1/2(1 ± 0.06)c^*$ is realized in ErAsS (Figure 2g). The magnetic structure evolution with an intermediate magnetic state indicates ErAsS is a highly fluctuated system, which is consistent with the geometry of this 3D spin-frustrated system. Specifically, the abrupt change of c^* component (from 0 to ½) in the propagation wave vector implies the variation of correlation from ferromagnetic to AFM. Substituting Er by rare-earth atoms with different anisotropy character could provide promising opportunities for magnetic-tuned phase transitions and new topological phases.

2.3. Electronic Structures of PM ErAsS

The electronic structure for PM ErAsS is studied by first-principles calculations, ARPES, and STS. The calculated band structure has essential anti-band crossings around Z and U points (**Figure 3**a,b). Without spin-orbit coupling (SOC), the band crossings form two Dirac nodal lines, which are fully gapped
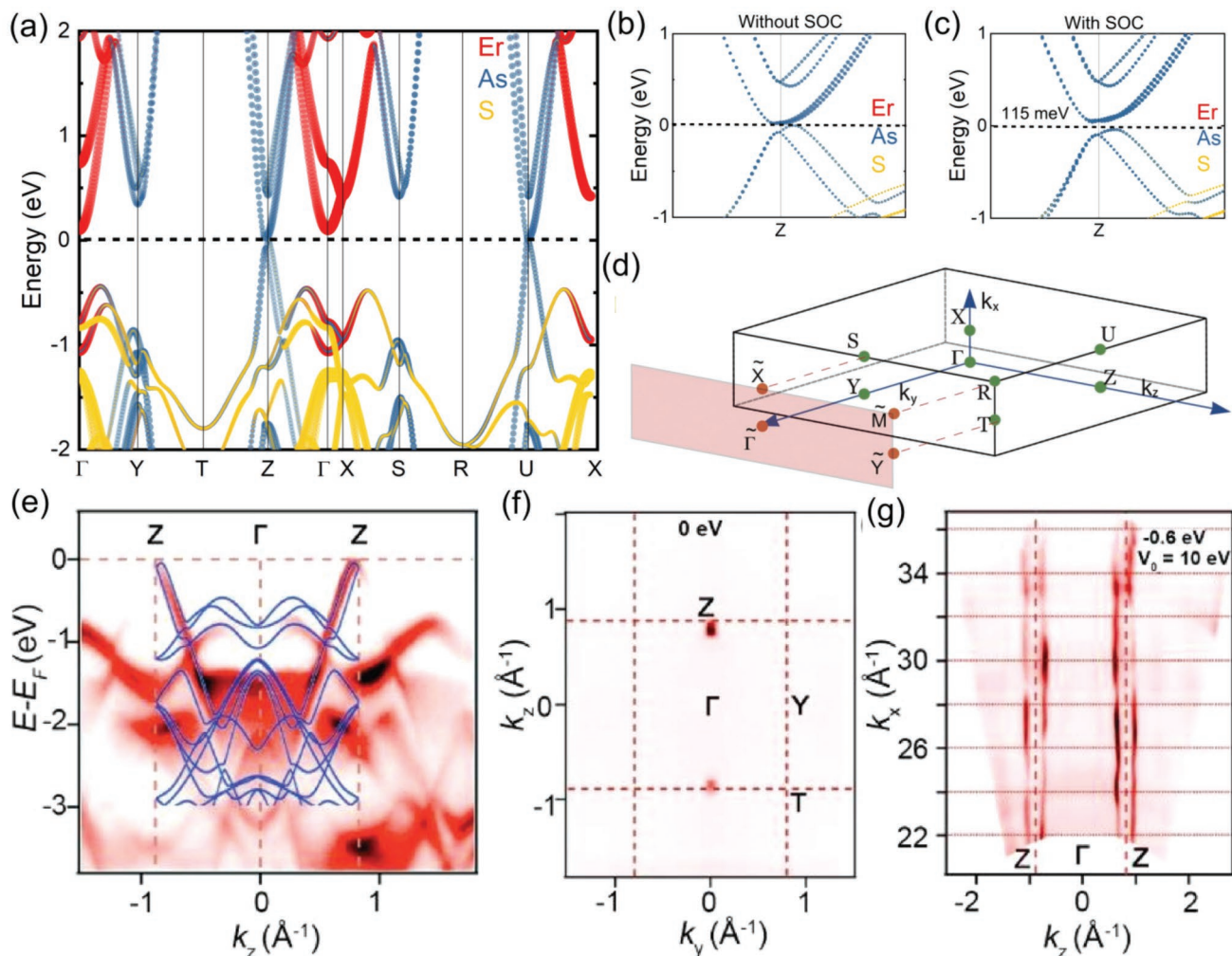
Figure 3. Comparison of calculated and measured electronic structure for PM ErAsS. a) Fat-band plot of the electronic band structure. Zoomed band structure around high-symmetry point Z b) without or c) with SOC. d) Brillouin zone (BZ) and projected surface BZ for (010) plane. e) ARPES intensity map along Z–Γ–Z. The solid blue curves are the calculated results. f) ARPES intensity map at E_F showing the Fermi surface in Z–Γ–Y plane. Red dashed lines denote the bulk BZ boundary. g) ARPES intensity map at $E = -0.6$ eV of X–Γ–Z plane measured with varying $h\nu$ from 70 to 200 eV. The inner potential is set to be 10 eV. The ARPES data in (e) and (f) are collected with $h\nu = 128$ eV.

under SOC. As shown in Figure 3c, the gap is 115 meV at Z point and 101 meV at U point (Figure S5, Supporting Information). Figure 3e shows the experimentally determined linear band dispersions near E_F along Z–Γ, which is normal to the (100) surface. The corresponding calculated bands are plotted as solid blue curves on top of the experimental data along Z–Γ–Z path. Figure 3f shows the intensity map at E_F measured on the (100) surface with tiny hole pocket observed around Z points, indicating a clean Fermi surface without any miscellaneous band dispersions. In Figure 3g, the constant energy contour of X–Γ–Z plane at $E = -0.6$ eV measured with varying photon energy ($h\nu$) is presented, unveiling the quasi-2D characteristic of ErAsS. These results indicate that the experimentally determined electronic bands are consistent with the calculations especially near E_F (Figure S9, Supporting Information, for more details of the electronic bands). Near E_F, a V-shaped dI/dV is revealed by STS (Figure S10, Supporting Information), which is commonly seen in Dirac materials.[50–52] Meanwhile, a narrow gap is observed with E_F located near the top of the band gap.

2.4. Discussion of Topological Properties

Symmetry indicators can be properly defined at fully gapped Dirac point for PM ErAsS with SOC. Due to the presence of inversion symmetry, the Z_4 indicator can be obtained by using the number of Kramer pairs with odd ($n_{\bar{K}}^-$) and even ($n_{\bar{K}}^+$) parity on eight time-reversal invariant momentum (TRIM) points.[17,53]

$$Z_4 = \sum_{K \in TRIM} \frac{n_K^- - n_K^+}{2} \mod 4 \qquad (1)$$

Space group $Pnma$ has three weak Z_2 indicators and one Z_4 indicator of inversion, which can be easily calculated as (0002). This nontrivial indicator reveals that ErAsS is a TCI. There are

**ADVANCED
SCIENCE NEWS**

www.advancedsciencenews.com

**ADVANCED
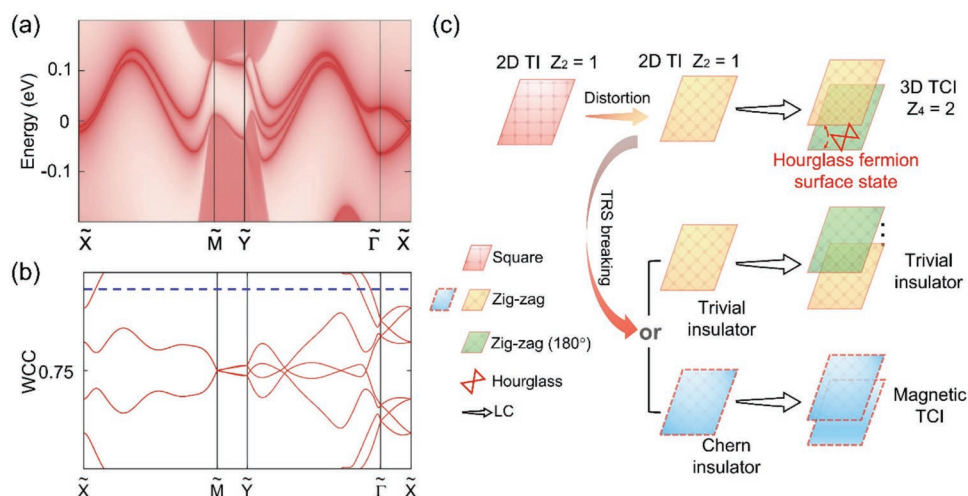MATERIALS**

www.advmat.de

Figure 4. Hourglass fermion surface state and magnetic-tuned exotic phases within LC scheme. a) Surface band structure of (010) plane with hourglass fermion surface state appearing on $\widetilde{\Gamma} - \widetilde{X}$. b) Spectrum of Wilson loop along high-symmetry lines. The loop is defined as a reciprocal lattice vector along [010]. The blue dashed line is chosen as the reference line. c) Schematic of exotic phases within LC scheme. 3D TCI with hourglass fermion surface state can be obtained by stacking 2D TIs of distortion-induced zig-zag As-atom plane with nonsymmorphic symmetry. By breaking TRS, 2D TI could be a trivial insulator or a Chern insulator. Multi-layered trivial insulator is still a trivial insulator, whereas multi-layered Chern insulator could be a magnetic TCI.

six kinds of topological invariants that can be defined in *Pnma* except weak topological invariants and an inversion invariant. Usually, they cannot be determined directly from symmetry-based indicators.

To get the knowledge of these topological invariants, we calculated the 2D surface states, which are determined by the first three topological invariants in Table S3, Supporting Information. The only nontrivial result appearing on the (010) surface is an hourglass fermion surface state along $\widetilde{\Gamma} - X$ (**Figure 4**a), with corresponding nonzero glide invariant $g^{001}_{\frac{1}{2}0\frac{1}{2}}$ (Table S3, Supporting Information). To confirm the nontrivial surface band connection, the Wilson loop[54] was calculated along the high-symmetry lines on the surface BZ (Figure 4b and Figure S6, Supporting Information). By choosing a reference line which only crosses the Wilson loop spectrum along $\widetilde{X} - \widetilde{M}$ and $\widetilde{Y} - \widetilde{\Gamma}$ (Figure 4b), the Wilson loop spectrum along $\widetilde{X} - \widetilde{M}$ is found to be twofold degenerated with $Z_4 = 2$,[55–57] corresponding to a nontrivial glide invariant (see detailed discussion in Supporting Information 4.2.). The bulk-boundary correspondence[58] reveals that the energy spectrum of Hamiltonian in the presence of a boundary is isomorphic to the spectrum of Wilson loop integrated along the direction perpendicular to the boundary. As the global gap is not obtained, the hourglass fermion surface state is confirmed in PM ErAsS. The mirror Chern number of ErAsS is calculated to be zero with trivial evolution of Wilson loop spectra for the subspace with mirror eigenvalue. Furthermore, 1D hinge states were predicted to be protected by 2_1-screw axes along the *a* and *b* axes with nonzero invariants $c^{100}_{\frac{1}{1}\frac{1}{2}\frac{1}{2}}$ and $c^{010}_{0\frac{1}{2}0}$ (Table S3, Supporting Information). As ErAsS is much more air stable than KHgX (X = As, Sb, and Bi)[20,21] and the Fermi surface is rather clean with a moderate gap ($\approx$100 meV), PM ErAsS could be a good candidate to experimentally observe the hourglass fermion surface state and explore high-order topological phases.[54,59] In the preliminary

experiment, a tiny hole pocket was observed, which inspired us to experimentally explore the hourglass fermion surface state in the near future through lifting the Fermi level by modifying the surface chemical potential or atomic termination.

The LC scheme is a theoretical method to classify TCIs by decomposing them into lower-dimensional blocks of topological states.[18,19] Considering the quasi-2D nature (Figure 3g) and the prominent contribution of As 4p orbitals to the anti-band crossings (Figure 3a) near E_F, we tried to understand the topological properties of ErAsS using LC scheme and found ErAsS being one of the experimental realization of LC scheme that maps the atomic layers in real space to the band topology in momentum space.[32] According to our calculation, the topological electronic structure of ErAsS can be fully described by one elementary LC, which is composed of two topological layers (100; 0) and $\left(100;\frac{1}{2}\right)$ in one unit cell (Table S4, Supporting Information). Thus, the two topological layers (100; 0) and $\left(100;\frac{1}{2}\right)$ coincide with the As-atom layers of ErAsS as illustrated in Figure 1a, showing the importance of As-atom layers in the formation of topological electronic bands. The distortion of As net induces the *a*-glide mirror plane perpendicular to the *c* axis, leading to the hourglass fermion surface state on the (010) surface, which is composed of glide-related Dirac cones induced by two topological layers. Therefore, the hourglass fermion surface state protected by the nonsymmorphic symmetry can be realized in a TCI candidate PM ErAsS (Figure 4c).

In the collinear AFM state, the energy level of 4f orbitals of Er locates about 0.5 eV above E_F, and the inversion symmetry $\mathcal{I}$ is not affected. A global gap along the high-symmetry lines can be clearly observed (Figure S7, Supporting Information). With all states doubly degenerated in BZ, Weyl nodes would not appear in this phase. The prominent anti-band crossing band structures can still be observed but now it is located around Γ due to the change of unit cell and the resulted band folding effect.

The symmetry indicator of this state and the mirror Chern number are calculated to be zero according to the magnetic topological quantum chemistry (MTQC) theory[31,58,60–62] and the Wilson loop spectrum[54,56] (Table S5 and Figure S8, Supporting Information), respectively. Thus, the hourglass fermion surface state is gapped. From the LC perspective, this can be understood by the fact that the 2D As-atom plane would translate to a trivial insulator under the magnetic structure provided by Er atoms (Figure 4c). For the same reason, the intermediate incommensurate magnetic states are also predicted to be trivial. Thus, there might exist a topological phase transition from the PM TCI with hourglass fermion surface state to an AFM trivial insulator, through an intermediate trivial state with breaking TRS, similar to the proposed topological phase transition driven by varying magnetic ordering in $EuIn_2As_2$.[63,64]

Considering the wavelike modulation which would give rise to a possible sinusoidal structure of Er moments and the highly fluctuating nature of ErAsS, various magnetic structures including ferromagnetism along the a axis could be realized by changing the rare-earth atoms or applying external magnetic field. Once the effective exchange field splitting on the As p-bands is competitive against the strength of band inversion, the As-atom layer can be tuned from 2D TI to a Chern insulator or a quantum anomalous Hall insulator.[65] In this case, the system might become a magnetic TCI with two elementary layers decorated by Chern insulators within the LC scheme (Figure 4c),[60] which provides an excellent opportunity for manipulating topological features through tuning the magnetic structures.

3. Conclusion

In conclusion, the crystal structure, magnetic structure, and topological properties of a TCI candidate ErAsS are studied. ErAsS crystalizes in an orthorhombic *Pnma* structure with distortion in the As-atom layer. The distortion results in a zig-zag-arranged As-atom layer and doubles the topological As-atom layer with nonsymmorphic symmetry. An evolution from PM to collinear AFM ground state through an intermediate incommensurate magnetic order is revealed. First-principles calculations, ARPES, and STS indicate a clean Fermi surface and linear bands with Dirac-like anti-band crossings near E_F in the PM phase. Further calculations show that PM ErAsS is a TCI candidate with hourglass fermion surface state protected by the crystalline symmetry. The incorporation of Er local moment breaks the time-reversal and glide symmetries, leading to a transition from a TCI in PM phase to a trivial insulator with collinear AFM state. Although the intermediate incommensurate magnetic state is a trivial insulator given the observed magnetic modulation, the magnetic fluctuation associated with the abrupt change in wavevectors suggests various magnetic structures, among which ferromagnetic order can be achieved and plausibly give rise to a magnetic TCI within LC scheme. ErAsS is to be one of the experimental realization of LC scheme that maps the atomic layers in real space to the band topology in momentum space. These results show ErAsS and related compounds could be a promising platform to unveil the physics of TCIs and investigate the interplay between magnetism and topology.

4. Experimental Section

Single Crystal Growth and Characterization: Single crystals of ErAsS were grown by the chemical vapor transport method. The as-received Er ingot (Alfa, 99.9%) was cut into small pieces, then mixed with As pieces (Alfa, 99.9999+%), S powder (Alfa, 99.9995%) in a mole ratio of 1:1:1, together with a small amount (≈100 mg) of I_2 (Alfa, 99.99+%) as the transport agent. These ingredients (≈2 g in total) were sealed in an evacuated silica tube (10 cm length; 1 cm inside diameter), heated to 1373/1223 K in a two-zone tube furnace over 10 h and held there for 10 days. Shiny, bright, and air-stable single crystals with plate shape as large as 2 mm × 2 mm × 0.1 mm were obtained at the low-temperature end. Single-crystal X-ray diffraction (SCXRD) was performed on a XtaLAB AFC12 (RCD3): Kappa single four-circle diffractometer at 297 K with multilayer mirror graphite-monochromatized Mo K_α radiation ($\lambda = 0.71073$ Å) operated at 50 kV and 40 mA. The HAADF images were collected on an ARM-200F (JEOL) high-resolution STEM operated at 200 kV with a CEOS Cs corrector (CEOS GmbH) to cope with the probe forming objective spherical aberration. The magnetic susceptibility and heat capacity measurements were carried out using a physical property measurement system (PPMS-9T, Quantum Design).

Magnetic Structure Characterization: Diffuse neutron scattering measurements were performed on the elastic diffuse scattering spectrometer, CORRELI, at the Spallation Neutron Source, Oak Ridge National Laboratory.[66] A white neutron beam with incident neutron energy from 10 to 200 meV was used. A large single crystal about 22.3 mg was cooled down with closed-cycle refrigerator and the data were collected at 2.22, 3.5, and 10 K. The single crystal was oriented with the [100] and [001] axes in the horizontal plane, and the diffraction pattern were measured in the (H0L) scattering plane by rotating the sample.

First-Principles Calculations: The first-principles calculations were performed by using the Vienna ab initio simulation Package (VASP)[67–69] and the generalized gradient approximation (GGA) with the Perdew–Burke–Ernzerhof (PBE) type exchange-correlation potential.[70,71] The cutoff energy of the plane-wave basis was 500 eV and the energy convergence standard was set to 10^{-7} eV. The 5 × 11 × 11 Γ centered K-point meshes were employed for the BZ sampling of the unit cell. The experimental crystal data were adopted to perform static calculations on ErAsS, taking into account both the PM and the collinear AFM configurations with or without SOC. Different pseudopotentials for Er with or without $4f$ electrons were adopted to simulate the PM phase and AFM phase, because the magnetism mainly comes from the $4f$ electrons. The on-site Coulomb interaction U = 6.0 eV[72] was adopted to produce the location of $4f$ electrons. The maximally localized Wannier functions[73] for $5d$ and $4f$ orbitals of Er, $4p$ orbitals of As, and $3p$ orbitals of S generated by Wannier90 Package[74] can well reproduce the first-principles electronic band structures. The tight binding (TB) model under Wannier basis and iterative Green's function method[75] were used to calculate the surface states. The hinge states of ErAsS were calculated by nanowire Hamiltonian constructed by the bulk TB model.

Electronic Structure Measurement: Synchrotron ARPES measurements on ErAsS were performed at the beamline 7.0.2, ALS, USA with a Scienta R4000 analyzer, and the "Dreamline" beamline at the Shanghai Synchrotron Radiation Facility (SSRF) with a Scienta DA30 analyzer. ErAsS single crystals were cleaved in situ along the (100) plane and measured at 30 K in a working vacuum better than 5 × 10^{-11} Torr. The STM/STS experiments were performed in a homebuilt low-temperature STM.

[CCDC 2128765 contains the supplementary crystallographic data for this paper. These data can be obtained free of charge from The Cambridge Crystallographic Data Centre via www.ccdc.cam.ac.uk/data_request/cif.]

Supporting Information

Supporting Information is available from the Wiley Online Library or from the author.

**ADVANCED
SCIENCE NEWS**

www.advancedsciencenews.com

**ADVANCED
MATERIALS**

www.advmat.de

Conflict of Interest

The authors declare no conflict of interest.

Data Availability Statement

The data that support the findings of this study are available from the corresponding author upon reasonable request.

[1] M. Z. Hasan, C. L. Kane, *Rev. Mod. Phys.* **2010**, *82*, 3045.
[2] X. L. Qi, S. C. Zhang, *Rev. Mod. Phys.* **2011**, *83*, 1057.
[3] F. Duncan, M. Haldane, *Rev. Mod. Phys.* **2017**, *89*, 045002.
[4] A. A. Burkov, L. Balents, *Phys. Rev. Lett.* **2011**, *107*, 127205.
[5] S. M. Young, S. Zaheer, J. C. Y. Teo, C. L. Kane, E. J. Mele, A. M. Rappe, *Phys. Rev. Lett.* **2012**, *108*, 140405.
[6] Z. J. Wang, Y. Sun, X. Q. Chen, C. Franchini, G. Xu, H. M. Weng, X. Dai, Z. Fang, *Phys. Rev. B* **2012**, *85*, 195320.
[7] Z. J. Wang, H. M. Weng, Q. S. Wu, X. Dai, Z. Fang, *Phys. Rev. B* **2013**, *88*, 125427.
[8] F. D. Tang, Y. F. Ren, P. P. Wang, R. D. Zhong, J. Schneeloch, S. Y. A. Yang, K. Yang, P. A. Lee, G. D. Gu, Z. H. Qiao, L. Y. Zhang, *Nature* **2019**, *569*, 537.
[9] S. H. Liang, J. J. Lin, S. Kushwaha, J. Xing, N. Ni, R. J. Cava, N. P. Ong, *Phys. Rev. X* **2018**, *8*, 031002.
[10] S. M. Chi, Z. L. Li, Y. Xie, Y. G. Zhao, Z. Y. Wang, L. Li, H. H. Yu, G. Wang, H. M. Weng, H. J. Zhang, J. Y. Wang, *Adv. Mater.* **2018**, *30*, 1801372.
[11] S. M. Chi, F. Liang, H. X. Chen, W. D. Tian, H. Zhang, H. H. Yu, G. Wang, Z. S. Lin, J. P. Hu, H. J. Zhang, *Adv. Mater.* **2020**, *32*, 1904498.
[12] C. Chen, Z. M. Yu, S. Li, Z. Y. Chen, X. L. Sheng, S. Y. A. Yang, *Phys. Rev. B* **2019**, *99*, 075131.
[13] L. Wu, F. Tang, X. G. Wan, *Phys. Rev. B* **2020**, *102*, 035106.
[14] S. S. Wang, Y. Liu, Z. M. Yu, X. L. Sheng, S. A. Yang, *Nat. Commun.* **2017**, *8*, 7.
[15] B. T. Fu, X. T. Fan, D. S. Ma, C. C. Liu, Y. G. Yao, *Phys. Rev. B* **2018**, *98*, 075146.
[16] M. Ezawa, *Phys. Rev. B* **2016**, *94*, 155148.
[17] Z. D. Song, T. T. Zhang, Z. Fang, C. Fang, *Nat. Commun.* **2018**, *9*, 3530.
[18] S. J. Huang, H. Song, Y. P. Huang, M. Hermele, *Phys. Rev. B* **2017**, *96*, 205106.
[19] H. Song, S. J. Huang, L. Fu, M. Hermele, *Phys. Rev. X* **2017**, *7*, 011020.
[20] Z. J. Wang, A. Alexandradinata, R. J. Cava, B. A. Bernevig, *Nature* **2016**, *532*, 189.
[21] J. Z. Ma, C. J. Yi, B. Q. Lv, Z. J. Wang, S. M. Nie, L. Wang, L. Y. Kong, Y. B. Huang, P. Richard, P. Zhang, K. Yaji, K. Kuroda, S. Shin, H. M. Weng, B. A. Bernevig, Y. Shi, T. Qian, H. Ding, *Sci. Adv.* **2017**, *3*, e1602415.
[22] M. Evain, L. Monconduit, A. Vanderlee, R. Brec, J. Rouxel, E. Canadell, *New J. Chem.* **1994**, *18*, 215.
[23] S. Li, Y. Liu, S. S. Wang, Z. M. Yu, S. Guan, X. L. Sheng, Y. G. Yao, S. Y. A. Yang, *Phys. Rev. B* **2018**, *97*, 045131.
[24] Y. G. Chen, Y. M. Lu, H. Y. Kee, *Nat. Commun.* **2015**, *6*, 6593.
[25] W. Tremel, R. Hoffmann, *J. Am. Chem. Soc.* **1987**, *109*, 124.
[26] L. M. Schoop, M. N. Ali, C. Strasser, A. Topp, A. Varykhalov, D. Marchenko, V. Duppel, S. S. P. Parkin, B. V. Lotsch, C. R. Ast, *Nat. Commun.* **2016**, *7*, 11696.
[27] S. Guan, Y. Liu, Z. M. Yu, S. S. Wang, Y. G. Yao, S. Y. A. Yang, *Phys. Rev. Mater.* **2017**, *1*, 054003.
[28] D. Takane, Z. W. Wang, S. Souma, K. Nakayama, C. X. Trang, T. Sato, T. Takahashi, Y. Ando, *Phys. Rev. B* **2016**, *94*, 121108.
[29] Y. Y. Lv, B. B. Zhang, X. Li, S. H. Yao, Y. B. Chen, J. Zhou, S. T. Zhang, M. H. Lu, Y. F. Chen, *Appl. Phys. Lett.* **2016**, *108*, 244101.
[30] M. R. van Delft, S. Pezzini, T. Khouri, C. S. A. Muller, M. Breitkreiz, L. M. Schoop, A. Carrington, N. E. Hussey, S. Wiedmann, *Phys. Rev. Lett.* **2018**, *121*, 256602.
[31] I. Lee, S. I. Hyun, J. H. Shim, *Phys. Rev. B* **2021**, *103*, 165106.
[32] Y. T. Qian, Z. Y. Tan, T. Zhang, J. C. Gao, Z. J. Wang, Z. Fang, C. Fang, H. M. Weng, *Sci. Chin. Phys., Mech. Astron.* **2020**, *63*, 107011.
[33] R. Singha, A. Pariari, B. Satpati, P. Mandal, *Phys. Rev. B* **2017**, *96*, 245138.
[34] A. Weiland, D. G. Chaparro, M. G. Vergniory, E. Derunova, J. Yoon, I. W. H. Oswald, G. T. McCandless, M. Ali, J. Y. Chan, *APL Mater.* **2019**, *7*, 101113.
[35] Y. Wang, Y. T. Qian, M. Yang, H. X. Chen, C. Li, Z. Y. Tan, Y. Q. Cai, W. J. Zhao, S. Y. Gao, Y. Feng, S. Kumar, E. F. Schwier, L. Zhao, H. M. Weng, Y. G. Shi, G. Wang, Y. T. Song, Y. B. Huang, K. Shimada, Z. Y. Xu, X. J. Zhou, G. D. Liu, *Phys. Rev. B* **2021**, *103*, 125131.
[36] M. M. Hosen, G. Dhakal, K. Dimitri, P. Maldonado, A. Aperis, F. Kabir, C. Sims, P. Riseborough, P. M. Oppeneer, D. Kaczorowski, T. Durakiewicz, M. Neupane, *Sci. Rep.* **2018**, *8*, 13283.
[37] L. M. Schoop, A. Topp, J. Lippmann, F. Orlandi, L. Muchler, M. G. Vergniory, Y. Sun, A. W. Rost, V. Duppel, M. Krivenkov, S. Sheoran, P. Manuel, A. Varykhalov, B. H. Yan, R. K. Kremer, C. R. Ast, B. V. Lotsch, *Sci. Adv.* **2018**, *4*, eaar2317.
[38] S. S. Yue, Y. T. Qian, M. Yang, D. Y. Geng, C. J. Yi, S. Kumar, K. Shimada, P. Cheng, L. Chen, Z. J. Wang, H. M. Weng, Y. G. Shi, K. H. Wu, B. J. Feng, *Phys. Rev. B* **2020**, *102*, 155109.
[39] R. S. K. Mong, A. M. Essin, J. E. Moore, *Phys. Rev. B* **2010**, *81*, 245209.
[40] C. Z. Chang, J. S. Zhang, X. Feng, J. Shen, Z. C. Zhang, M. H. Guo, K. Li, Y. B. Ou, P. Wei, L. L. Wang, Z. Q. Ji, Y. Feng, S. H. Ji, X. Chen, J. F. Jia, X. Dai, Z. Fang, S. C. Zhang, K. He, Y. Y. Wang, L. Lu, X. C. Ma, Q. K. Xue, *Science* **2013**, *340*, 167.

[41] C. Z. Chang, W. W. Zhao, D. Y. Kim, H. J. Zhang, B. A. Assaf, D. Heiman, S. C. Zhang, C. X. Liu, M. H. W. Chan, J. S. Moodera, *Nat. Mater.* **2015**, *14*, 473.

[42] J. H. Li, Y. Li, S. Q. Du, Z. Wang, B. L. Gu, S. C. Zhang, K. He, W. H. Duan, Y. Xu, *Sci. Adv.* **2019**, *5*, eaaw5685.

[43] C. Liu, Y. C. Wang, H. Li, Y. Wu, Y. X. Li, J. H. Li, K. He, Y. Xu, J. S. Zhang, Y. Y. Wang, *Nat. Mater.* **2020**, *19*, 522.

[44] P. Y. Wang, J. Ge, J. H. Li, Y. Z. Liu, Y. Xu, J. Wang, *Innovation* **2021**, *2*, 100098.

[45] R. Ceolin, N. Rodier, P. Khodadad, *J. Less-Common Met.* **1977**, *53*, 137.

[46] P. Gambardella, S. Rusponi, M. Veronese, S. S. Dhesi, C. Grazioli, A. Dallmeyer, I. Cabria, R. Zeller, P. H. Dederichs, K. Kern, C. Carbone, H. Brune, *Science* **2003**, *300*, 1130.

[47] E. Garcia-Matres, J. L. Martinez, J. Rodriguez-Carvajal, *European Phys. J. B* **2001**, *24*, 59.

[48] Y. A. Izyumov, V. E. Naish, V. N. Syromiatnikov, *J. Magn. Magn. Mater.* **1979**, *12*, 249.

[49] Y. A. Izyumov, V. E. Naish, S. B. Petrov, *J. Magn. Magn. Mater.* **1979**, *13*, 267.

[50] W. B. Li, L. J. Kong, C. Y. Chen, J. Gou, S. X. Sheng, W. F. Zhang, H. Li, L. Chen, P. Cheng, K. H. Wu, *Sci. Bull.* **2018**, *63*, 282.

[51] Q. Zhong, J. Zhang, P. Cheng, B. J. Feng, W. B. Li, S. X. Sheng, H. Li, S. Meng, L. Chen, K. H. Wu, *J. Phys.-Condes. Matter* **2017**, *29*, 095002.

[52] S. Y. Li, K. K. Bai, W. J. Zuo, Y. W. Liu, Z. Q. Fu, W. X. Wang, Y. Zhang, L. J. Yin, J. B. Qiao, L. He, *Phys. Rev. Appl.* **2018**, *9*, 054031.

[53] L. Fu, C. L. Kane, *Phys. Rev. B* **2007**, *76*, 045302.

[54] F. Schindler, A. M. Cook, M. G. Vergniory, Z. J. Wang, S. S. P. Parkin, B. A. Bernevig, T. Neupert, *Sci. Adv.* **2018**, *4*, eaat0346.

[55] K. Shiozaki, M. Sato, K. Gomi, *Phys. Rev. B* **2016**, *93*, 195413.

[56] B. J. Wieder, B. Bradly, Z. J. Wang, J. Cano, Y. Kim, H. S. D. Kim, A. M. Rappe, C. L. Kane, B. A. Bernevig, *Science* **2018**, *361*, 246.

[57] A. Alexandradinata, Z. J. Wang, B. A. Bernevig, M. Zaletel, *Phys. Rev. B* **2020**, *101*, 235166.

[58] R. Yu, X. L. Qi, A. Bernevig, Z. Fang, X. Dai, *Phys. Rev. B* **2011**, *84*, 075119.

[59] F. Schindler, Z. J. Wang, M. G. Vergniory, A. M. Cook, A. Murani, S. Sengupta, A. Y. Kasumov, R. Deblock, S. Jeon, I. Drozdov, H. Bouchiat, S. Gueron, A. Yazdani, B. A. Bernevig, T. Neupert, *Nat. Phys.* **2018**, *14*, 918.

[60] B. R. Peng, Y. Jiang, Z. Fang, H. M. Weng, C. Fang, *arXiv:2102.12645*, **2021**.

[61] Y. F. Xu, L. Elcoro, Z. D. Song, B. J. Weider, M. G. Vergniory, N. Regnault, Y. L. Chen, C. Felser, B. A. Bernevig, *Nature* **2020**, *586*, 702.

[62] L. Elcoro, B. J. Weider, Z. D. Song, Y. F. Xu, B. Bradlyn, B. A. Bernevig, *Nat. Commun.* **2021**, *12*, 5965.

[63] Y. F. Xu, Z. D. Song, Z. J. Wang, H. M. Weng, X. Dai, *Phys. Rev. Lett.* **2019**, *122*, 256402.

[64] S. X. M. Riberolles, T. V. Trevisan, B. Kuthanazhi, T. W. Heitmann, F. Ye, D. C. Johnston, S. L. Bud'ko, D. H. Ryan, P. C. Canfield, A. Kreyssig, A. Vishwanath, R. J. McQueeney, L. L. Wang, P. P. Orth, B. G. Ueland, *Nat. Commun.* **2021**, *12*, 999.

[65] R. Yu, W. Zhang, H. J. Zhang, S. C. Zhang, X. Dai, Z. Fang, *Science* **2010**, *329*, 61.

[66] F. Ye, Y. H. Liu, R. Whitfield, R. Osborn, S. Rosenkranz, *J. Appl. Crystallogr.* **2018**, *51*, 315.

[67] G. Kresse, J. Hafner, *Phys. Rev. B* **1993**, *47*, 558.

[68] G. Kresse, J. Furthmuller, *Comp. Mater. Sci.* **1996**, *6*, 15.

[69] G. Kresse, J. Furthmuller, *Phys. Rev. B* **1996**, *54*, 11169.

[70] J. P. Perdew, K. Burke, M. Ernzerhof, *Phys. Rev. Lett.* **1997**, *78*, 1396.

[71] S. Grimme, *J. Comput. Chem.* **2006**, *27*, 1787.

[72] S. L. Dudarev, G. A. Botton, S. Y. Savrasov, C. J. Humphreys, A. P. Sutton, *Phys. Rev. B* **1998**, *57*, 1505.

[73] I. Souza, N. Marzari, D. Vanderbilt, *Phys. Rev. B* **2002**, *65*, 035109.

[74] A. A. Mostofi, J. R. Yates, Y. S. Lee, I. Souza, D. Vanderbilt, N. Marzari, *Comput. Phys. Commun.* **2008**, *178*, 685.

[75] M. P. L. Sancho, J. M. L. Sancho, J. Rubio, *J. Phys. F-Met. Phys.* **1985**, *15*, 851.